Adaptive Genetic Algorithm Enabled Tailoring of Piezoelectric Metamaterials for Optimal Vibration Attenuation

Yupei Jian[1], Lihua Tang*[1], Guobiao Hu*[2], Yuesheng Wang[3], Kean C Aw[1]

[1] Department of Mechanical Engineering, The University of Auckland, Auckland 1010, New Zealand

[2] School of Civil and Environmental Engineering, Nanyang Technological University, Singapore 639798, Singapore

[3] School of Mechanical Engineering, Tianjin University, Tianjin 300350, China

*Correspondence authors: l.tang@auckland.ac.nz (Tang); guobiao.hu@ntu.edu.sg (Hu)

Abstract

Piezoelectric metamaterials with shunt resonant circuits have been extensively investigated for their tunability in bandgaps. However, the vibration attenuation ability induced by the electromechanical coupling is generally weaker than that of mechanical metamaterials, limiting their applications in engineering practice. This research presents a non-uniform piezoelectric metamaterial beam with shunt circuit parameters optimized by an adaptive genetic algorithm for tailoring the vibration attenuation zone. First, the non-uniform piezoelectric metamaterial beam is modeled for transmittance analysis and verified by the finite element method. By simultaneously tuning the resonance frequencies and the resistance of the shunt circuits, it is conceptually demonstrated that the attenuation zone can be broadened, and the undesired localized vibration modes can be mitigated. Subsequently, two optimization strategies are proposed respectively for two typical vibration scenarios. The inductances and the load resistance in the shunt circuits constitute the set of design variables and are optimized by the adaptive genetic algorithm. Dedicated case studies are carried out, and the results show that the objective-oriented circuitry parameters can greatly enrich the design freedom, and tailor the transmittance profile according to a given vibration spectra. As compared to the conventional uniform and the graded piezoelectric metamaterial beams, the proposed design provides superior vibration attenuation performance and demonstrates a promising approach for tailoring piezoelectric metamaterials systems.

Keywords: Piezoelectric Metamaterial, Optimization, Adaptive Genetic Algorithm, Tailored Transmittance

1. Introduction

Since the very first local resonance (LR) phononic crystal (metamaterial) was proposed by Liu et al. [1], this class of artificially engineered periodic material/structure opened a new way to manipulate acoustic/elastic waves by virtue of their LR bandgaps (i.e., the specific frequency band in which waves cannot propagate). The LR bandgap differentiates itself from the traditional Bragg scattering bandgap [2] by being able to form within the sub-wavelength region, making metamaterials suitable for low-frequency vibration/noise control [3].

Research efforts have been devoted to tailoring the LR bandgap in recent years. Various types of purely mechanical metamaterials, based on, but not limited to, mechanical resonators such as small beams [4-6], cavities and Helmholtz resonators [7-10], membranes and rings [11-13], circular metal bars [14], origamis [15, 16] have been proposed. However, except for some scalable mechanical metamaterials, such as an origami-based metamaterial that possesses a deformable geometry through coordinated folding, most mechanical metamaterials' bandgap properties can hardly be modified after being manufactured. By using piezoelectric shunt circuit techniques [17], piezoelectric metamaterials received extensive attention due to their tuneability in the bandgap. Specifically, piezoelectric materials/elements with shunting circuits are integrated into the host structure, enabling us to customize the bandgap width and location by changing the circuitry parameters [18]. Thorp *et al.* [19] presented the first piezoelectric metamaterial by periodically attaching piezoelectric patches with inductance shunt circuits to a rod. Analogous to the mechanical resonators, LR bandgap is generated due to the circuit resonance. However, the electromechanical coupling effect generated by the pure inductance shunt circuit is normally weak, limiting the attenuation in a narrow frequency band [20]. To broaden the bandgaps of piezoelectric metamaterials, various shunt circuits have been proposed, including negative capacitance circuits [21, 22], amplifier-resonator feedback circuits [23, 24], programmable digital circuits [25, 26], and nonlinear switching circuits [27, 28]. Although enlarged bandgaps are realized, costly additional devices and equipment are required to implement those complex circuitry, hindering their applications in practice.

The abovementioned work mainly focuses on the metamaterial with a periodically arranged array of resonators. More recently, near-periodic metamaterials, in which material or geometric properties are slightly varying in space, have been emerging with promising potential for enhancing vibration attenuation performance. Fabro *et al.* [29] comprehensively investigated the influence of varying material and geometric parameters due to the manufacturing tolerances on the attenuation performance of a multi-frequency metastructure. A stochastic model

according to the given variability levels was proposed. It showed that even a small level of variability might enhance or reduce the bandgap width and attenuation ability. Similar conclusions were drawn in [30], which suggested that further optimization for the variabilities is necessary to capture the favorable factors. Except for the random variability of system properties, graded metamaterials emerge as a hot research topic for broadband vibration attenuation. A deterministic function to specify the graded variation in the resonance frequencies of the local resonators forms the key of this design strategy. This concept has been implemented for lattice type metamaterials [31], beam/plate-like metamaterials with mechanical resonators [32-34]. It was found that the widths of the bandgaps can be significantly widened by properly tuning the local resonance frequency array while the attenuation strength is inevitably weakened. Recently, a graded piezoelectric metamaterial with shunt resonant circuits [35, 36] is investigated. Due to the tunability of the shunt circuit, the grading cell is easier to implement and can avoid introducing mass variation. However, the wave propagation characteristics of graded metamaterials depend on the deterministic grading function, which is limited to monotonically increasing (ascending) or decreasing (descending) of the local resonance frequency array. Additionally, due to the break of periodicity, a unique phenomenon called wave localization/trapping [37] occurs. Wave localization leads to the concentration of vibration energy at different sections of a host structure as the excitation frequency varies. This energy concentration effect can be exploited for energy harvesting [38, 39], and the spatial-spectral wave selection behavior has a great potential for wave filtering/waveguide applications [40, 41]. Though the vibration attenuation region opened in a graded metamaterial is usually wide, there often appear many wave localization modes-related resonant peaks inside. Those resonant peaks split the vibration attenuation region into pieces and make it discontinuous. The large vibrational deformation associated with these modes is detrimental to broadband vibration attenuation. Therefore, from the perspective of vibration attenuation, the wave localization modes should be avoided or controlled [42].

Apart from the abovementioned aperiodic designs obtained by trial and error, optimization algorithm-assisted designs have also been reported in the existing literature. Gao *et al.* [43] optimized the geometric parameters of a hybrid porous metamaterial using the teaching learning-based optimization method and increased the sound absorption coefficient. He *et al.* [44] employed a data-driven optimization method to improve the noise reduction ability of a periodic beam with multiple acoustic black holes. In addition to these optimization algorithms, the genetic algorithm (GA) has received enormous attention because of its ability to quickly

search for near-global optimal solutions, which implies that GA is especially suitable for handling multimodal function models [45]. Wu *et al.* [46] focused on optimizing the mass distribution of a mechanical metamaterial with the aid of GA. Six independent variables were optimized, and the bandgap width was increased by 123.5% after optimization. Similar work can also be found in [47], which assumed the design variables in the form of sine function coefficients to reduce the number of variables. In summary, the above optimization studies were all conducted on mechanical metamaterials and focused on tuning their geometric, material, or structural parameters.

In this work, we present a novel optimal piezoelectric metamaterial with shunt resonant circuits. Unlike designs using stochastic models or grading functions, the circuit parameters of each shunt circuit of the metamaterial system could be arbitrary and are optimized by an genetic algorithm. As a result, the number of design variables, i.e., design freedom, is considerably expanded. A set of inductor values and a resistor value are chosen as the design variables due to their direct effects on the circuit resonance frequencies and the resonance strengths. Due to the relatively large variable space in this study, the conventional GA is prone to get trapped in a local extremum [48]. To avoid getting stuck on a local optimum, we employ an adaptive genetic algorithm (AGA) [49], which can adjust its crossover and mutation rate adaptively in the iterative process to conserve population diversity, making the results closer to the global optimum. The main optimization objective is to enhance the overall vibration attenuation strength of the piezoelectric metamaterial in a target frequency region. Without loss of generality, two typical vibration scenarios, namely, band-limited white noise and colored noise excitations, are considered. Correspondingly, two AGA-based optimization strategies are proposed. Dedicated case studies are conducted to illustrate the dynamic behavior of the optimized piezoelectric metamaterial. It shows that tailored wave attenuation properties can be achieved to adapt to the given vibration spectra.

The article is structured as follows. Section 2 commences with the derivation of the dimensionless analytical model of the non-uniform piezoelectric metamaterial beam and the analytical solution of transmittance, followed by the validation using the finite element method. The effect of non-uniform resonant shunt circuits and external load resistance on the formation of broadband pseudo-bandgap is also discussed in this section. Section 3 presents two optimization functions according to the considered vibration scenarios. An adaptive genetic algorithm is employed to solve the optimization functions. Several case studies are presented in Section 4. The main conclusions from this work are summarized in Section 5.

2. Theoretical Foundation

2.1 Model Description

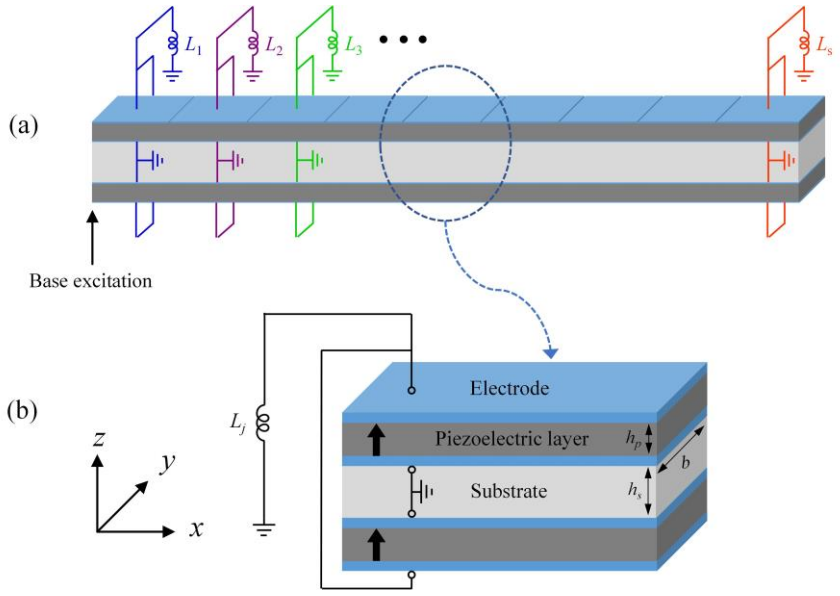

Figure 1. Schematic diagram of the piezo-meta-beam: (a) global view; (b) close-up view of a unit cell.

Figure 1.(a) shows the piezoelectric metamaterial beam (piezo-meta-beam) under the base excitation. The top and bottom surfaces of the piezoelectric layers are covered by *S* pairs of electrodes. Each electrode pair is connected in parallel to a shunt circuit. It is noteworthy that various shunt circuits have been proposed to broaden the bandgap widths of piezoelectric metamaterials, as mentioned in Section 1. Since this work focuses on tailoring the bandgaps to enhance the overall attenuation performance, a simple inductive shunt circuit is considered as proof of concept. The close-up view of a unit cell in **Figure 1**.(b) illustrates the implementation of the electrodes and the shunt circuit. A synthetic inductor circuit [50] can be implemented to facilitate the inductance tuning. Sugino et al. [51] studied a uniform piezo-meta-beam shunted to identical resonant circuits. The reaction moment generated by the piezoelectric element when *L*-*C* resonance occurs neutralizes the bending moment in the substrate, thus preventing wave propagation. Unlike the previous study [51], the strict periodicity is omitted in terms of the shunt circuit design, though the geometries of the cells are kept identical in this work. In other words, the shunt circuits connected to those cells are allowed to be different to permit more design freedom. The shunt circuits will be tuned according to predefined optimization objective functions for different excitation scenarios. With the assumption of a slender beam, an analytical model of the piezo-meta-beam is developed using Euler-Bernoulli beam theory

to predict the transmittance. The governing equation for the transverse motion of the metamaterial beam can be written as [51]

$$\rho A\frac{\partial^2 w(x,t)}{\partial t^2}+EI\frac{\partial^4 w(x,t)}{\partial x^4}-\theta\sum_{j=1}^{S}v_j(t)\frac{\partial^2}{\partial x^2}[H(x-x_j^L)-H(x-x_j^R)]=\rho A a_{cc}e^{i\omega t} \quad (1)$$

and the governing equation for the shunt circuit can be written as the following differential equation according to Kirchhoff's current law:

$$C_{p,j}\frac{dv_j(t)}{dt}+Y_j v_j(t)+\theta\int_{x_j^L}^{x_j^R}\frac{\partial^3 w(x,t)}{\partial x^2\partial t}dx=0 \quad (2)$$

where $w(x,t)$ represents the transverse deflection of the beam relative to a time-dependent harmonic base excitation $w_b(t)=W_b e^{i\omega t}$. For brevity, a conceptually equivalent acceleration field $a_{cc}=-\omega^2 W_b$ is used to represent the base motion. $v_j(t)$ is the voltage across the jth electrode pair, and Heaviside function $H(x)$ is used to indicate the area of each electrode pair along the length of the piezoelectric layer. x_j^L and x_j^R denote the left and right ends of the jth electrode, respectively. Y_j denotes the external admittance shunted to the jth electrode pair. Besides, EI is the effective bending stiffness in the short-circuit condition, and ρA is the effective mass per unit length of the piezo-meta-beam:

$$EI=E_s I_s+E_p I_p \quad (3)$$

$$\rho A=b\left(\rho_s h_s+2\rho_p h_p\right) \quad (4)$$

where E, ρ and h are the elastic modulus, density, and thickness, respectively. The subscripts s and p denote the substrate material and the piezoelectric material, respectively. $I_s=\frac{bh_s^3}{12}$ and $I_p=\frac{2b}{3}\left(\left(h_p+\frac{h_s}{2}\right)^3-\frac{h_s^3}{8}\right)$ respectively denote the area moments of inertia of the substrate and piezoelectric layers. The substrate and piezoelectric layers have the same width b. θ is the electromechanical coupling coefficient of the beam, and $C_{p,j}$ is the internal capacitance of jth segment of the piezoelectric layers which are electrically in parallel:

$$\theta=\frac{e_{31}b}{2h_p}\left[\left(h_p+\frac{h_s}{2}\right)^2-\frac{h_s^2}{4}\right] \quad (5)$$

$$C_{p,j} = \frac{2\varepsilon_{33}^{S} b\left(x_j^R - x_j^L\right)}{h_p} \tag{6}$$

where e_{31} is the piezoelectric coefficient and ε_{33}^{S} is the permittivity at the constant strain of the piezoelectric material. Furthermore, the resonance frequency of the *L*-*C* circuit for the *j*th unit cell can be expressed as $\omega_j = 1/\sqrt{L_j C_{p,j}}$. Thus, Eq. (2) is rewritten as

$$\frac{1}{\omega_j^2 L_j}\frac{dv_j(t)}{dt} + Y_j v_j(t) + \theta \int_{x_j^L}^{x_j^R} \frac{\partial^3 w(x,t)}{\partial x^2 \partial t} dx = 0 \tag{7}$$

To generalize the analysis presented in this study, the governing equations are rendered in the non-dimensional form by scaling the displacement *w* and coordinate *x* with the length of the beam L_s, and the time with the characteristic time τ_c:

$$\tilde{w} = \frac{w}{L_s}, \xi = \frac{x}{L_s}, \tau = \frac{t}{\tau_c} \tag{8}$$

where $\tau_c = \frac{1}{\omega_c} = \sqrt{\frac{\rho A L_s^4}{EI}}$. The governing equations are non-dimensionalized to take the form:

$$\frac{\partial^2 \tilde{w}(\xi,\tau)}{\partial \tau^2} + \frac{\partial^4 \tilde{w}(\xi,\tau)}{\partial \xi^4} - \sum_{j=1}^{S} \tilde{v}_j(\tau) \frac{\partial}{\partial \xi}\left[\delta\left(\xi - \xi_j^L\right) - \delta\left(\xi - \xi_j^R\right)\right] = \tilde{a}_{cc} e^{i\Omega\tau} \tag{9}$$

$$\frac{1}{\tilde{\omega}_j^2 \tilde{L}_j}\frac{d\tilde{v}_j(\tau)}{d\tau} + \tilde{Y}_j \tilde{v}_j(\tau) + \int_{\xi_j^L}^{\xi_j^R} \frac{\partial^3 \tilde{w}(\xi,\tau)}{\partial \xi^2 \partial \tau} d\xi = 0 \tag{10}$$

with the following dimensionless parameters:

$$\tilde{v}_j = v_j \Big/ \left(\frac{EI}{\theta L_s}\right),\ \tilde{a}_{cc} = \frac{a_{cc}}{L_s \omega_c^2},\ \tilde{L}_j = L_j \Big/ \left(\frac{EI}{\theta^2 L_s \omega_c^2}\right),\ \tilde{Y}_j = \frac{EI}{\theta^2 L_s \omega_c} Y_j,\ \Omega = \frac{\omega}{\omega_c},\ \tilde{\omega}_j = \frac{\omega_j}{\omega_c} \tag{11}$$

2.2 Transmittance Analysis

Using the modal superposition method and ignoring the contribution of high-frequency modes, the transverse vibration of the metamaterial beam can be expressed as the sum of the contributions of the first *N* modes:

$$\tilde{w}(\xi,\tau) = \sum_{r=1}^{N} \phi_r(\xi)\eta_r(\tau)\ \ (r = 1,2,3...) \tag{12}$$

where $\phi_r(\xi)$ is the dimensionless *r*th mode shape of the metamaterial beam under the short-circuit condition. Considering the boundary conditions of a cantilever beam, $\phi_r(\xi)$ is normalized to take the form as:

$$\phi_r(\xi) = \cosh\beta_r\xi - \cos\beta_r\xi - \frac{\sinh\beta_r - \sin\beta_r}{\cosh\beta_r + \cos\beta_r}\left(\sinh\beta_r\xi - \sin\beta_r\xi\right) \tag{13}$$

$\eta_r(\tau)$ is the dimensionless modal coordinate. Since only the steady-state response is of interest, it is assumed in the form of $\eta_r(\tau) = H_r e^{i\Omega\tau}$ under the harmonic base excitation. H_r denotes the amplitude of the modal coordinate of the *r*th mode. The mode shape can be normalized using the orthogonality conditions:

$$\int_0^1 \phi_r(\xi)\phi_k(\xi)\,d\xi = \delta_{rk} \tag{14}$$

$$\int_0^1 \frac{d^4\phi_r(\xi)}{d\xi^4}\phi_k(\xi)\,d\xi = \hat{\omega}_r^2\delta_{rk} \tag{15}$$

where δ_{rk} is the Kronecker delta function. $\hat{\omega}_r$ is the dimensionless linear natural frequency of the beam, which can be obtained as $\hat{\omega}_r = \frac{\omega_r}{\omega_c} = \beta_r{}^2\sqrt{\frac{EI}{\rho AL_s^4}}\frac{1}{\omega_c} = \beta_r{}^2$. Substituting Eq. (12) into Eq. (9), multiplying by $\phi_k(\xi)$, integrating over the substrate length from ξ = 0 to ξ = 1, applying the orthogonality conditions, and introducing modal viscous damping, we can obtain the dimensionless modal governing equation as:

$$\ddot{\eta}_k(\tau) + 2\zeta_k\hat{\omega}_k\dot{\eta}_k(\tau) + \hat{\omega}_k^2\eta_k(\tau) - \sum_{j=1}^{S}\left[\tilde{v}_j(\tau)\Delta\phi_k'(\xi_j)\right] = \tilde{a}_{cc}e^{i\Omega\tau}\int_0^1\phi_k(\xi)\,d\xi \tag{16}$$

where $\Delta\phi_k'(\xi_j) = \phi_k'(\xi_j^R) - \phi_k'(\xi_j^L)$ and the prime represents the derivative with respect to ξ. ζ_k is the modal damping ratio. Taking the Laplace transform of Eq. (16), one can obtain:

$$\left(\hat{\omega}_k^2 - \Omega^2 + 2i\zeta_k\hat{\omega}_k\Omega\right)H_k - \sum_{j=1}^{S}\left[\tilde{V}_j\Delta\phi_k'(\xi_j)\right] = \tilde{a}_{cc}\int_0^1\phi_k(\xi)\,d\xi \tag{17}$$

where $\tilde{V}_j$ is the steady-state amplitude of $\tilde{v}_j(\tau)$. Then, substituting Eq. (12) into Eq. (10) and taking the Laplace transform yields

$$\frac{i\Omega}{\tilde{\omega}_j^2\tilde{L}_j}\tilde{V}_j + \tilde{Y}_j\tilde{V}_j + i\Omega\sum_{r=1}^{N}\Delta\phi_r'(\xi_j)H_r = 0 \tag{18}$$

Note that in the physical implementation of the equivalent inductance shown in **Figure 1**, it is difficult to obtain a pure inductive reactance using a synthetic circuit, and an additional parasitic resistance would be inevitably introduced [52, 53]. Therefore, we consider a resistor R in series with the inductor, and the impedance is given by $\tilde{Y}_j = 1\Big/\left(\tilde{R} + i\Omega\tilde{L}_j\right)$, in which $\tilde{R} = R\Big/\left(\dfrac{EI}{\theta^2 L_s \omega_c}\right)$ is the dimensionless resistance. It should be pointed out that the resonance frequency of the *L*-*R*-*C* circuit in the *j*th cell is changed to $\omega_j = \sqrt{1\Big/\left(L_j C_{p,j}\right) - \left(R\Big/L_j\right)^2}$. Since the value of the internal capacitance $C_{p,j}$ is very small compared to L_j and R, the high-order term $\left(R\Big/L_j\right)^2$ is negligible compared to the first-order term $1\Big/\left(L_j C_{p,j}\right)$. Therefore, the resonance frequency ω_j is approximately unchanged and still $\omega_j = 1\Big/\sqrt{L_j C_{p,j}}$.

The steady-state amplitude of the dimensionless voltage $\tilde{V}_j$ can be calculated from Eq. (18). Substituting $\tilde{V}_j$ into Eq. (17) yields

$$\left(\hat{\omega}_k^2 - \Omega^2 + 2i\zeta_k\hat{\omega}_k\Omega\right)H_k + \sum_{j=1}^{S}\frac{i\Omega}{\dfrac{1}{\left(\tilde{R} + i\Omega\tilde{L}_j\right)} + \dfrac{i\Omega}{\tilde{\omega}_j^2\tilde{L}_j}}\Delta\phi_k'\left(\xi_j\right)\sum_{r=1}^{N}\Delta\phi_r'\left(\xi_j\right)H_r = \tilde{a}_{cc}\int_0^1\phi_k\left(\xi\right)d\xi \tag{19}$$

Rearranging Eq. (19) in the matrix form yields:

$$\mathbf{CH} = \mathbf{F} \tag{20}$$

where

$$\mathbf{C} = \begin{bmatrix} c_{11} & c_{12} & \cdots & c_{1m} & \cdots & c_{1N} \\ c_{21} & c_{22} & \cdots & c_{2m} & \cdots & c_{2N} \\ \cdots & \cdots & \cdots & \cdots & \cdots & \cdots \\ c_{k1} & c_{k2} & \cdots & c_{km} & \cdots & c_{kN} \\ \cdots & \cdots & \cdots & \cdots & \cdots & \cdots \\ c_{N1} & c_{N2} & \cdots & c_{Nm} & \cdots & c_{NN} \end{bmatrix}, \mathbf{H} = \begin{bmatrix} H_1 \\ H_2 \\ \cdots \\ H_k \\ \cdots \\ H_N \end{bmatrix}, \mathbf{F} = \begin{bmatrix} f_1 \\ f_2 \\ \cdots \\ f_k \\ \cdots \\ f_N \end{bmatrix} \tag{21}$$

and

$$c_{k,m}=\begin{cases}1+\sum_{j=1}^{S}\dfrac{\dfrac{i\Omega}{\left(\hat{\omega}_k^2-\Omega^2+2i\zeta_k\hat{\omega}_k\Omega\right)}}{\left(\dfrac{1}{\left(\tilde{R}+i\Omega\tilde{L}_j\right)}+\dfrac{i\Omega}{\tilde{\omega}_j^2\tilde{L}_j}\right)}\Delta\phi_k'\left(\xi_j\right)\Delta\phi_m'\left(\xi_j\right) & \text{for } k=m\\ \sum_{j=1}^{S}\dfrac{\dfrac{i\Omega}{\left(\hat{\omega}_k^2-\Omega^2+2i\zeta_k\hat{\omega}_k\Omega\right)}}{\left(\dfrac{1}{\left(\tilde{R}+i\Omega\tilde{L}_j\right)}+\dfrac{i\Omega}{\tilde{\omega}_j^2\tilde{L}_j}\right)}\Delta\phi_k'\left(\xi_j\right)\Delta\phi_m'\left(\xi_j\right) & \text{for } k\neq m\end{cases} \tag{22}$$

and

$$f_k=\frac{\tilde{a}_{cc}\int_0^1\phi_k\left(\xi\right)d\xi}{\left(\hat{\omega}_k^2-\Omega^2+2i\zeta_k\hat{\omega}_k\Omega\right)} \tag{23}$$

This allows us to obtain the modal coordinate vector **H** by solving Eq. (20). Substituting the solved **H** into Eq. (12), the steady-state amplitude $\tilde{W}\left(\xi,\Omega\right)$ of the relative transverse vibration $\tilde{w}$ can finally be calculated. The transmittance of the piezo-meta-beam is defined as below to indicate the vibration attenuation performance.

$$\tau\left(\Omega\right)=20\log\left(\frac{\left|\tilde{W}_{abs}\left(1,\Omega\right)\right|}{\left|-\tilde{a}_{cc}/\Omega^2\right|}\right)\text{dB} \tag{24}$$

where $\tilde{W}_{abs}\left(\xi,\Omega\right)=\tilde{W}\left(\xi,\Omega\right)-\tilde{a}_{cc}/\Omega^2$ denotes the amplitude of the absolute transverse deflection of the beam. Eq. (24) describes the ratio between the amplitude of the tip displacement (i.e., ξ = 1) of the metamaterial beam to the amplitude of the base motion. $\tau\left(\Omega\right)<0$ indicates that the tip displacement is smaller than the base displacement, implying that vibration is attenuated.

2.3 Finite Element Verification

In this section, the analytical model is verified by the finite element method. It is known that the conventional piezo-meta-beam with identical shunt resonant circuits (uniform piezo-meta-beam, for short) can produce a single bandgap due to local resonance. The bandgap width is strongly related to the resonance frequency (i.e., $\tilde{\omega}_1$) of the uniform resonant circuit [54], given by

$$\sqrt{\alpha}\tilde{\omega}_1 < \Omega < \tilde{\omega}_1 \tag{25}$$

where the constant coefficient $\alpha = \dfrac{\left(1-k_{31}^2\right)E_pI_p + E_sI_s}{E_pI_p + E_sI_s}$ stands for the ratio between the effective bending stiffnesses of the piezo-meta-beam in short-circuit and open-circuit conditions. $k_{31} = d_{31}\sqrt{\dfrac{E_p}{\varepsilon_{33}^T}} = \sqrt{\dfrac{e_{31}^2}{e_{31}^2 + \varepsilon_{33}^S E_p}}$ is the electromechanical coupling coefficient of the piezoelectric material.

Table 1. Parameters of the piezo-meta-beam

Substrate – Aluminum	
Density ρ_s	2700 kg/m^3
Young's modulus E_s	69 GPa
Thickness h_s	1 mm
Width b	10 mm
Substrate length L_s	200 mm
Piezoelectric layer – PZT-5H	
Young's modulus in short circuit E_p	60.6 GPa
Density ρ_p	7500 kg/m^3
Piezoelectric coefficient e_{31}	-16.61 C/m^2
Permittivity ε_{33}^S	2.5554e-08 F/m
Thickness h_p	0.6 mm

To illustrate the merit of non-uniform design in terms of vibration attenuation, we consider the metamaterial beam with varying circuit resonance frequencies by connecting different inductors to the cells. In the numerical examples, we adopt a bimorph piezo-meta-beam made of Aluminium substrate and two PZT-5H piezoelectric layers. 10 electrode pairs with uniform length are exerted on the two surfaces of the piezoelectric layer. The material and geometric parameters of the system are listed in **Table 1**. Different inductances are assigned to the 10 shunt circuits for ensuring that the resonance frequencies of the 1st to the 10th shunt circuits are: 150 Hz, 148 Hz, 146 Hz, …, 132 Hz, respectively. Note that this non-uniform design with gradually varied shunt circuits of different resonance frequencies is a so-called graded metamaterial. One can refer to the relevant literature [31, 32, 35, 36] for more information on this recently developed broadband vibration attenuation technique. The dynamic response of the uniform piezo-meta-beam shunted to 10 identical *L*-*R* circuits with 150 Hz resonance frequency is also given for comparison. In addition, the modal damping ratio is set to 0.001. In order to demonstrate the resonant peaks formed due to the introduction of non-uniform

inductances and compare the results of the analytical and finite element models, a small resistance $R = 1\ \Omega$ (here Ω is the unit of resistance) is considered first to remove the effect of electrical damping. The finite element software package COMSOL 5.3 is used to simulate the corresponding metamaterial beams. The models are meshed with 10172 elements and 187672 degrees of freedom to ensure convergence.

Figure 2 shows that the simulation results by the finite element model are in good agreement with the theoretical predictions. It should be pointed out that the resonant peaks calculated by the analytical model and finite element model are slightly different (see the enlarged view in **Figure 2(b)).** This is caused by the plane-stress assumption [55] in the modeling stage, which reduces the 3D constitutive equations of the piezoelectric material into 1D (i.e., 31-mode). From **Figure 2,** it can be seen that the width from the left boundary to the right boundary of the bandgap generated by the non-uniform metamaterial beam is wider than that of the uniform counterpart, implying that it is possible to further extend the bandgap by properly tuning the resonance frequency of each unit cell. However, as shown in the enlarged view in **Figure 2(b)**, multiple undesired resonant peaks emerge when varying the resonance frequencies. This phenomenon can be interpreted by that a few transverse waves with frequencies in the bandgap region are not attenuated but reflected and transmitted, resulting in a localization vibration mode [56].

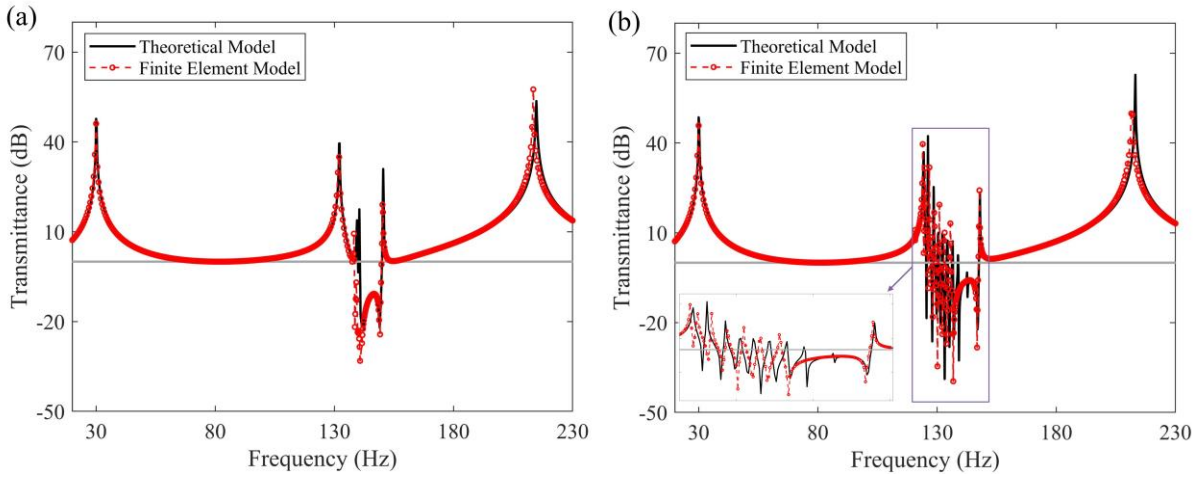

Figure 2. Comparison between the transmittances calculated by the analytical and finite element models: (a) uniform piezo-meta-beam; (b) non-uniform piezo-meta-beam.

To further reveal the effect of the localization vibration modes on the bandgap formation, the dispersion relation of an infinitely long metamaterial beam with varying resonance frequencies is also numerically obtained by finite element method using COMSOL 5.3. Dispersion relation (i.e., a relation between the Bloch wavenumber q and frequency) is a powerful tool to capture

bandgaps, and it is also known as the band structure in the field of metamaterials. The infinitely long beam is achieved by applying the Floquet-Bloch boundary condition on the two ends of a superlattice that contains 10 cells. With the same arrangement of the resonance frequency array, **Figure 3** shows the dispersion relation of the superlattice metamaterial beam. The horizontal axis of **Figure 3** denotes the normalized wave number ($q^* = qL_s/\pi$), where $0 < q^* < 1$ indicates the irreducible Brillouin zone. Note that only the real solution of q is plotted, while the imaginary q indicates an evanescent wave that will decay quickly when it propagates along the beam. From **Figure 3**, it is confirmed that several passbands appear within the upper and lower dispersion curves due to the variation of resonance frequencies of the shunt circuits. Those passbands split the single bandgap into multiple discrete bandgaps (i.e., the shaded areas in grey). From the perspective of broadband vibration attenuation, these passbands are undesired.

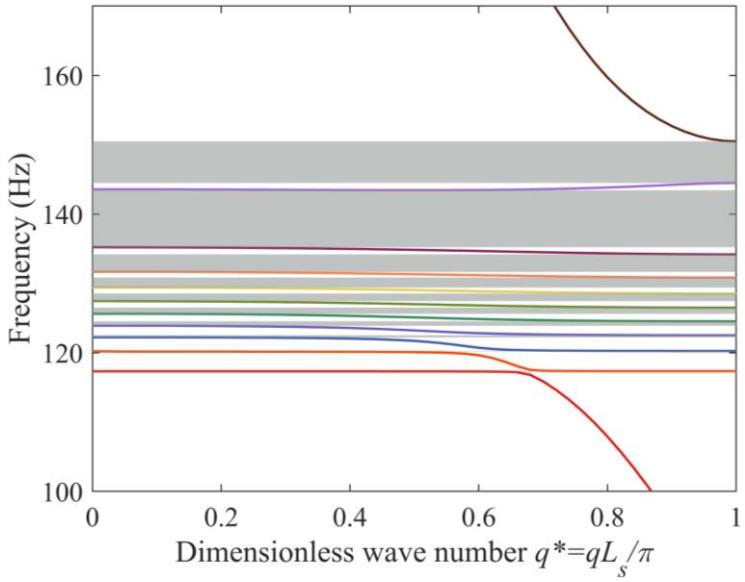

Figure 3. Dispersion relation of the superlattice metamaterial structure obtained by the finite element method. Multiple bandgaps emerge due to the variation of the circuit resonance frequencies. The discrete bandgaps inside the attenuation region are shaded in grey.

According to the conclusions in [57], the resistors connected to the electrode pairs play the role of electrical damping and could give rise to a metadamping phenomenon when combined with the local resonance mechanism. Therefore, it is natural to introduce proper resistance to eliminate the localization mode-induced resonant peaks. Here, **Figure 4** presents the transmittance of the non-uniform metamaterial beam with a larger load resistance (R = 800 Ω).

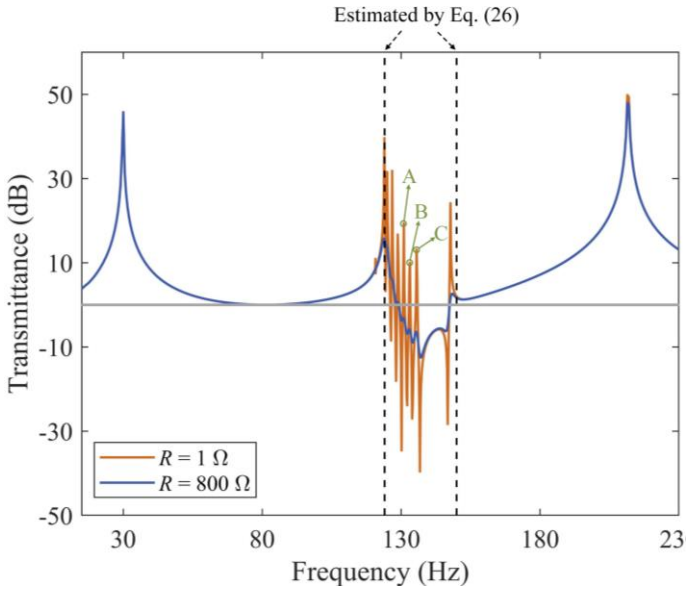

Figure 4. Transmittances of the non-uniform piezo-meta-beam obtained by the finite element method for R =1 Ω and R = 800 Ω. The dashed lines denote the predicted attenuation region by Eq. (26). Note that for R = 800 Ω, the resonant peaks are significantly reduced, forming a wide pseudo bandgap.

As expected, the localization mode-induced resonant peaks are remarkably suppressed, and a continuous vibration attenuation region is achieved when a large resistance is used. Note that bandgap is generally defined in the band structure, which refers to a frequency range within which no real solution of Bloch wavenumber exists. Thus, the continuous attenuation region obtained here using a large resistance is actually a pseudo bandgap. The analytical expression of this pseudo bandgap of the non-uniform metamaterial is derived. Generally, for the metamaterial containing S cells with S local resonance frequencies (i.e., $\tilde{\omega}_1, \tilde{\omega}_2, ...\tilde{\omega}_j, ...\tilde{\omega}_S$), S independent bandgaps associated with the resonance frequency array can be calculated according to Eq. (25). Therefore, it is reasonable to predict that the pseudo bandgap of the non-uniform piezo-meta-beam falls into the below range:

$$\sqrt{\alpha}\left(\tilde{\omega}_j\right)_{\min} \le \Omega \le \left(\tilde{\omega}_j\right)_{\max} \tag{26}$$

where the subscripts min and max respectively denote the minimum and maximum values of the resonance frequencies $\tilde{\omega}_j$ of the shunt circuits. To verify Eq. (26), we plot the edge frequencies predicted by Eq. (26) in **Figure 4** (i.e., dashed lines). As expected, the vibration is attenuated in the predicted pseudo bandgap.

Furthermore, **Figure 5** shows the steady-state response of the graded metamaterial beam at selected excitation frequencies, which correspond to the resonant peaks (A, B, and C) marked in the transmittance plot in **Figure 4.** The colored bar scales the total deformation of the

metamaterial beam along the *x*-direction. It can be seen in **Figure 5(a)** that the wave localization occurs around the middle of the beam. As a comparison, **Figure 5(b)** shows that flexural waves are dramatically attenuated, which explains why the large electrical damping can significantly suppress the localization mode-induced resonant peaks.

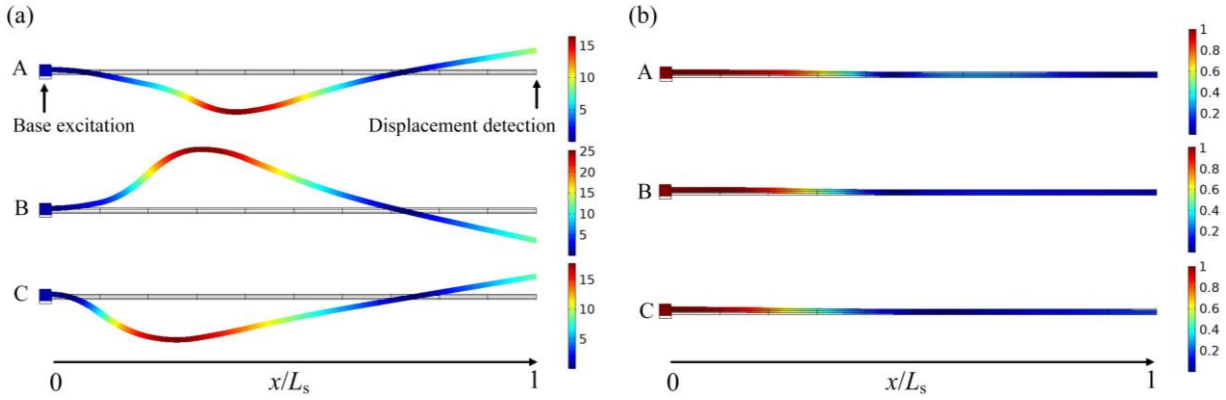

Figure 5. Vibration modes of the non-uniform piezo-meta-beam at the frequencies of three localization modes: (a) R = 1 Ω; (b) R = 800 Ω. A, B, and C represent the selected frequencies in Figure 4.

In summary, the above analysis shows that broadband vibration attenuation of the piezo-meta-beam is achievable by combining varying local resonance frequencies and proper resistance. However, the above non-uniform metamaterial beam is just a special arrangement that requires the variation to be monotonically increasing or decreasing. Therefore, a concern is raised that the graded metamaterial can hardly handle a variety of vibration sources featured with different frequency spectra. In this study, we aim to leverage the advantage of the non-uniform design of the piezo-meta-beam by tuning the resonant shunt circuits in a disordered pattern. Specifically, an adaptive genetic algorithm-based optimization approach is proposed to determine the resonance frequencies of the shunt circuits. The superiority of the tailored piezo-meta-beam with disordered resonance frequencies (tailored piezo-meta-beam, for short) over the conventional uniform piezo-meta-beam as well as the graded piezo-meta-beam will be illustrated in Section 4.

3. Optimization Strategies

With the developed theoretical model, this section focuses on the optimization strategies to enhance the overall vibration attenuation performance of the non-uniform piezo-meta-beam and make it adaptive to different vibration scenarios. In many industrial circumstances, vibrations are often random and dominant in certain frequency spectra. In this section, we consider two typical random excitations, i.e., band-limited white noise excitation and band-

limited colored noise excitation. Based on the previous discussion, we select the inductances of the shunt circuits as the design variables for broadening the attenuation region. Additionally, the resistance in the shunt circuit is also taken into consideration due to its ability to flatten resonant peaks.

3.1 Band-limited white noise excitation

The vibration energy of a band-limited white noise spreads evenly over a certain spectrum, i.e., the power spectral density of the noise signal is constant over a limited frequency range. With this type of excitation, it is inappropriate to evaluate the attenuation effect of the metamaterial beam by either the maximum attenuation strength or the bandwidth. In the literature, average transmittance, which describes the average attenuation strength, is adopted as an indicator to quantify the overall attenuation performance [32, 47]. The average transmittance of the piezo-meta-beam over the frequency range of interest (i.e., $\mathbf{\Psi} = \left[\Omega_A,\ \Omega_B\right]$) is given by:

$$\tau_{avg} = \frac{1}{\Omega_B - \Omega_A}\int_{\Omega_A}^{\Omega_B} \tau\left(\Omega\right) d\Omega \tag{27}$$

Note that $\tau\left(\Omega\right)$ is the transmittance function as defined by Eq. (24). It is time-consuming to integrate $\tau\left(\Omega\right)$ from Ω_A to Ω_B. Instead, the integral can be discretely approximated by

$$\tau_{avg} = \frac{1}{\Omega_B - \Omega_A}\sum_{j=1}^{M}\left[\tau\left(\Omega_A + j\Delta\Omega\right)\Delta\Omega\right] \tag{28}$$

where $\Delta\Omega$ represents the frequency interval and $M = \left(\Omega_B - \Omega_A\right)/\Delta\Omega$. The optimization objective function is set to minimize the average transmittance in the prescribed frequency range of interest:

$$J_1 = \min\left[\tau_{avg}\left(\tilde{\mathbf{L}}, \tilde{R}, \mathbf{\Psi}\right)\right] \tag{29}$$

where $\tilde{\mathbf{L}} = \left(\tilde{L}_1, \tilde{L}_2, ...\tilde{L}_S\right)$ is the vector of S design variables $\tilde{L}_j$, j = 1, 2, …, S, which are the dimensionless inductances of the S shunt resonant circuits. $\tilde{R}$ is the dimensionless resistance, which is the (S+1)th design variable. For all the shunt circuits, $\tilde{R}$ is assumed to be the same. To improve the optimization efficiency, more constraints should be considered to limit the design space. On the one hand, the attenuation region of the non-uniform piezo-meta-beam is roughly located in the pseudo bandgap predicted by Eq. (26). Hence, it is straightforward to deduce the constraints as $\left(\tilde{\omega}_j\right)_{\max} \le \Omega_B$ and $\sqrt{\alpha}\left(\tilde{\omega}_j\right)_{\min} \ge \Omega_A$. Recalling the relationship between $\tilde{\omega}_j$ and $\tilde{L}_j$, one can convert the above inequalities into the constraints for $\tilde{\mathbf{L}}$. On the

other hand, a suitable load resistance should be considered to suppress the peaks inside the attenuation region, as discussed in Section 2.3. However, an excessive resistance may weaken the local resonance effect of shunting circuits [58], which indicates $\tilde{R}$ should not be tuned too large. These constraints on the variables $\left(\tilde{\mathbf{L}}, \tilde{R}\right)$ limit the design space as:

$$\begin{aligned} s.t. \quad & \frac{1}{\Omega_B^2 \tilde{C}_p} \le \tilde{\mathbf{L}} \le \frac{\alpha}{\Omega_A^2 \tilde{C}_p} \\ & \tilde{R}_l \le \tilde{R} \le \tilde{R}_u \end{aligned} \tag{30}$$

3.2 Band-limited colored noise excitation

The vibration energy of another type of random vibration, i.e., band-limited colored noise excitation, also spreads over a limited frequency range, but the power spectral density is not constant. Similarly, the average transmittance is used as the Figure of merit to guide the optimization of the piezo-meta-beam to adapt to this type of excitation. Since the excitation intensity varies over the spectrum, we are naturally motivated to endow the piezo-meta-beam with a frequency-dependent attenuation strength according to the spectral density profile [36]. To this end, the transmittance function $\tau\left(\Omega\right)$ in Eq. (28) should be multiplied by a weighting function $\lambda(\Omega)$.

$$\tau_{avg,c} = \frac{1}{\Omega_B - \Omega_A} \sum_{j=1}^{M} \left[\lambda\left(\Omega\right) \tau\left(\Omega_A + j\Delta\Omega\right) \Delta\Omega \right] \tag{31}$$

where the weighting function $\lambda\left(\Omega\right),\ \Omega \subset \mathbf{\Psi}$ can be determined by fitting the envelope of the power spectral density profile of the target excitation. It is worth noting that Eq. (31) is valid since the piezo-meta-beam under investigation is assumed to be a linear system that obeys the linear superposition assumption. The optimization objective function is thus obtained as

$$J_2 = \min\left[\tau_{avg,c}\left(\tilde{\mathbf{L}}, \tilde{R}, \mathbf{\Psi}\right) \right] \tag{32}$$

Besides, the same constraints in Eq. (30) are applied to the design variables.

3.3 Adaptive genetic algorithm method

In this work, the genetic algorithm (GA) is employed to solve the optimization problems with specified objectives J_1 and J_2. The principle of the conventional GA is to simulate the natural evolution process where the fittest individuals have more chances to produce offspring of the next generation, and the individuals progressively evolve toward better solutions. The evolution process starts with a randomly generated initial population, i.e., a matrix $\mathbf{X}^{(S+1)\times Q}$ that consists of a series of variable vectors subjected to the constraint conditions Eq. (30). The

variable vector $\left(\tilde{\mathbf{L}},\tilde{R}\right)$ with (S+1) dimensions represents an individual from the initial population with the size of Q. The optimization objectives Eqs. (29) and (32) are directly used as fitness functions to evaluate the qualities of the individuals. According to the obtained fitness values, three operators, namely, selection, crossover, and mutation, are applied to the individuals in the population to reproduce better offspring. Subsequently, a new generation is obtained, and the above procedure is repeated. After successive iterations, when no better generation can be produced, the optimal solution is obtained. In [47], the optimization of a rainbow metamaterial was performed by using the conventional GA to determine the optimal masses of local resonators. The problem in the current work is more complicated since we have many more design variables (i.e., S+1 variables) than in [47] (4 variables). The conventional GA may easily fall into a local extremum [48]. Hence, an adaptive genetic algorithm (AGA) [49] is adopted to avoid getting stuck in a local extremum. The most significant difference of the AGA from the conventional GA is that new crossover (P_c) and mutation operators (P_m) are adaptive rather than fixed probabilities. The adaptive crossover (P_c) and mutation operators are defined as:

$$P_c=\begin{cases} k_1\left(1-\dfrac{\arcsin\left(f_{avg}/f_{\max}\right)}{\pi/2}\right) & \arcsin\left(\dfrac{f_{avg}}{f_{\max}}\right)\geq\pi/6 \\ k_2\dfrac{\arcsin\left(f_{avg}/f_{\max}\right)}{\pi/2} & \arcsin\left(\dfrac{f_{avg}}{f_{\max}}\right)<\pi/6 \end{cases} \tag{33}$$

$$P_m=\begin{cases} k_3\dfrac{\arcsin\left(f_{avg}/f_{\max}\right)}{\pi/2} & \arcsin\left(\dfrac{f_{avg}}{f_{\max}}\right)\geq\pi/6 \\ k_4\left(1-\dfrac{\arcsin\left(f_{avg}/f_{\max}\right)}{\pi/2}\right) & \arcsin\left(\dfrac{f_{avg}}{f_{\max}}\right)<\pi/6 \end{cases} \tag{34}$$

where f_{avg} and $f_{\max}$, respectively, denote the average and maximum fitness values of the individuals in one generation. $\arcsin\left(f_{avg}/f_{\max}\right)$ is the indicator to judge whether the population is concentrated or dispersed. k_1 to k_4 are constant values. In this study, k_1=1, k_2 =2, k_3 =0.02, k_4 =0.05. The adaptability of AGA makes it more robust and can avoid falling into a local extremum. Thus, it is more applicable to handle a complicated problem with a large volume of datasets. **Algorithm** below describes the procedure of the AGA-assisted optimization method.

Algorithm AGA-assisted optimization for non-uniform piezo-meta-beam

Input: g_{max} = Maximum number of iterations
Q = Quantity of the individual
γ = Fitness function based on Eq. (29) or (32)
Output: δ = Optimal variables $\left(\mathbf{L}, \tilde{R}\right)$; $\boldsymbol{f}_{opt}$ = Optimal fitness value subsets

Initialization x=Initialize random $(S+1)\times Q$ dimensions population subjected to Eq. (30)
$\boldsymbol{f}$ = Fitness(**x**, γ) \\Calculate fitness values for the population
while ($g \le g_{max}$) **do** \\Maximum iterations are not meet
    $g = g+1$
    P_c = Update crossover probability according to Eq. (33)
    P_m = Update mutation probability according to Eq. (34)
    while ($j \le Q$) **do** \\Not updated all individuals
        $j = j+1$
        Select individuals from **x** according to $\boldsymbol{f}$ \\Apply selection operator
        Cross the individuals according to P_c \\Apply crossover operator
        Mutate the individuals according to P_m \\Apply mutation operator
    end while
    x = Update the population
    $\boldsymbol{f}$ = Fitness(**x**, γ) \\Calculate fitness values for the new generation
    $\boldsymbol{f}_{opt}$ = Maximum($\boldsymbol{f}$) \\Save the best fitness value in current generation
end while
δ = Migrate the individual with the best fitness value from **x**
Return(δ, $\boldsymbol{f}_{opt}$)

*Phrases and sentences after double-slash are comments.

4. Case Studies

This section presents several optimization case studies under the aforementioned two types of excitations. The objective of this section is twofold: (1) to validate the feasibility of the proposed optimization strategies; (2) to demonstrate the superiority of the tailored piezo-meta-beam over the uniform and the graded ones. The geometric and material parameters of the piezo-meta-beam are listed in **Table 1**.

4.1 Optimization for band-limited white noise excitation

In the first case study, we employ the proposed strategy to optimize the piezo-meta-beam for suppressing a band-limited white noise excitation. The optimization objective J_1 in Eq. (29) is used as the fitness function. The frequency range of interest is assumed to be [170 Hz, 200 Hz], which can be non-dimensionalized into $\boldsymbol{\Psi} = \left[19.8, 23.3\right]$. The number of electrodes is considered as S = 10, leading to 11 design variables. Based on Eq. (30), the constraint for the inductances is calculated to be $0.00280 < \tilde{\mathbf{L}} < 0.00388$, i.e., 37.1 H < L_j < 51.4 H. In addition, the constraint for the load resistance is chosen to be $0.000069 < \tilde{R} < 0.000699$, i.e., 50 Ω < R

< 500 Ω. The quantity of the individuals is set to Q = 80. **Figure 6** shows the fitness value evolution in the optimization process. It can be found the fitness value progressively converges during the optimization process. After dozens of iterations, the convergence is achieved, and the optimal solution is obtained.

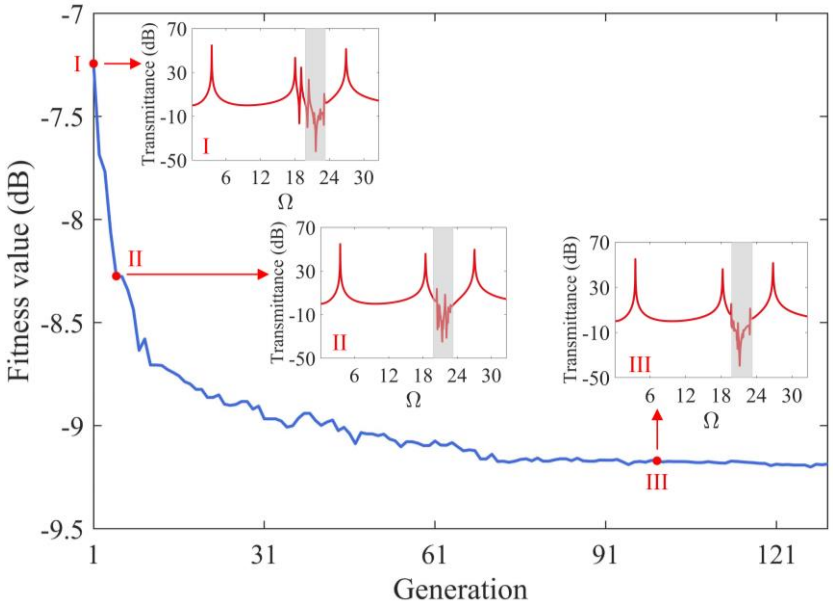

Figure 6. Fitness value evolution during the optimization process of the piezo-meta-beam subject to the band-limited white noise excitation. Subfigures I, II, and III show the transmittance responses with the best fitness values in Generations 1, 5, and 100. The grey shaded regions in the subfigures denote the frequency range of interest $\boldsymbol{\Psi}$.

Below lists the optimal dimensionless system parameters for the tailored piezo-meta-beam:

$$\tilde{\mathbf{L}} = \begin{bmatrix} 0.00303,\ 0.00275,\ 0.00353,\ 0.00317,\ 0.00308, \\ 0.00298,\ 0.00309,\ 0.00332,\ 0.00330,\ 0.00357 \end{bmatrix}; \qquad (35)$$
$$\tilde{R} = 0.000071$$

To clearly show the evolution of the attenuation region, the transmittance responses of the piezo-meta-beam with the best fitness values from the selected Generations 1, 5, and 100 are displayed as the subfigures in **Figure 6**. The target frequency range $\boldsymbol{\Psi}$ is shaded in grey. It is observed that the transmittance profile inside the attenuation region gradually evolves, and the valley becomes deeper during the optimization process.

In addition, the effect of the number of design variables on the efficiency of the optimization process is investigated. Sugino *et al.* [51] discussed the relation between the bandgap formation and the number of electrodes for the uniform piezoelectric metamaterial. It shows that the appearance of bandgap requires a certain number of electrodes, while excessive electrodes do not contribute significantly to the bandgap width or the attenuation intensity. We investigate

three additional cases with different numbers of electrodes, namely, S = 5, S=16, and S = 25, indicating 6, 17, and 26 design variables, respectively. The length of the piezoelectric segment L_s/S changes accordingly. It is well known that genetic algorithms are time-consuming, and most computational resources are spent on repeated calculation of the fitness values. Therefore, the convergence time of the algorithm strongly depends on the population scale ($(S+1)\times Q$ dimensions) and the complexity of the fitness function. In our cases, the efficiency of the optimization algorithm is evaluated by the effective generation G_{eff}, which is defined as the generation when the change in the best fitness value for each of the previous 20 adjacent generations is less than 0.3%. A smaller G_{eff} means faster convergence in a shorter time. **Figure 7** shows the calculated effective generation G_{eff} for the cases with different S. The best fitness values obtained in those cases are also plotted. It can be found that the increase of design variables results in a slower convergence speed (i.e., a larger effective generation) but a smaller best fitness value. It took respectively 1.2, 5.8, 15.2, and 35 minutes for the study cases with S = 5, 10, 16, and 25 to converge. Therefore, there is a trade-off between the optimal solution and the computational cost and S = 10 is adopted throughout the work.

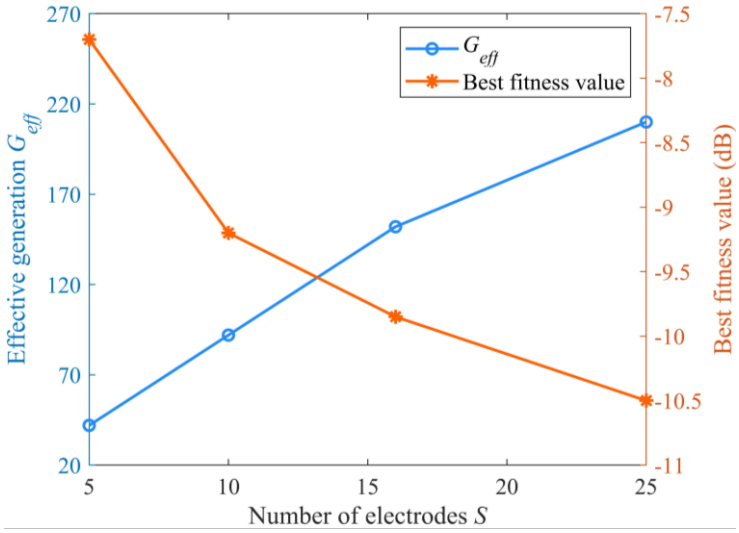

Figure 7. Evolution of the effective generation (left y-axis) and the corresponding best fitness value (right y-axis) for different numbers of electrodes S = 5, 10, 16, and 25.

Then, the transmittance of the tailored piezo-meta-beam is compared with those of the plain beam (i.e., all the piezoelectric segments are short-circuited), the uniform piezo-meta-beam, and the graded piezo-meta-beam to reveal its superiority. Notably, the vibration attenuation performance of a graded metamaterial depends on the predefined grading scheme. According to [35], the best attenuation performance of a graded piezo-meta-beam is achieved by adopting

the first-order descending scheme, which is adopted in this work for comparison. The grading scheme is [35]:

$$\tilde{\omega}_{t,j} = \tilde{\omega}_t + \Delta\tilde{\omega} - 2\Delta\tilde{\omega}\left(\frac{j-1}{S-1}\right) \tag{36}$$

where $\tilde{\omega}_t$ is the dimensionless center frequency of the resonance frequency array $\tilde{\omega}_{t,j}$, j=1, 2, ..., S. $\Delta\tilde{\omega}$ is the dimensionless first-order frequency spacing, which is set positive to ensure that the resonance frequencies are arranged in descending order. For a fair comparison, the AGA-based optimization is also conducted for the uniform piezo-meta-beam with design variables ($\tilde{L}$, $\tilde{R}$) and the graded piezo-meta-beam with design variables ($\tilde{\omega}_t$, $\Delta\tilde{\omega}$, $\tilde{R}$) to seek their optimal configurations. For the uniform metamaterial, its optimal system parameters are determined to be ($\tilde{L}$, $\tilde{R}$) = (0.00304, 0.000166). The optimal system parameters of the graded metamaterial are determined to be ($\tilde{\omega}_t$, $\Delta\tilde{\omega}$, $\tilde{R}$) = (22.37, 0.59, 0.000115). **Figure 8** compares the transmittances of these models. The dashed curve in **Figure 8** represents the transmittance of the plain beam.

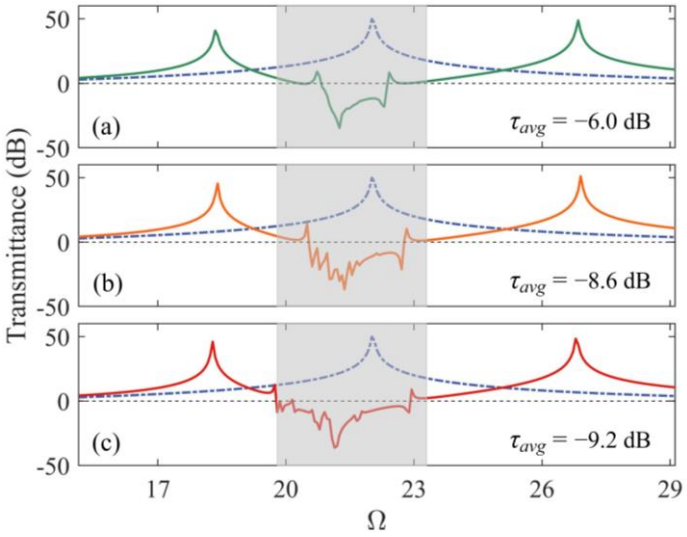

Figure 8. Comparison of the transmittance responses of (a) uniform piezo-meta-beam, (b) graded piezo-meta-beam and (c) tailored piezo-meta-beam.

The uniform piezo-meta-beam produces a narrow bandgap in the target frequency range (i.e., the grey area), as shown in **Figure 8**(a). The average transmittance of the uniform model is τ_{avg} = −6.0 dB. As shown in **Figure 8**(b), the graded piezo-meta-beam produces a wider bandgap than the uniform model, while the attenuation valley depth is almost the same as that of the uniform model. Moreover, as compared to the uniform model, the average transmittance of the graded one is reduced to τ_{avg} = −8.6 dB, representing a 43.4% improvement. **Figure 8**(c)

illustrates the transmittance of the tailored piezo-meta-beam. It can be observed that the attenuation region produced by the tailored model almost covers the entire target frequency range $\boldsymbol{\Psi}$. Moreover, the bottom of the valley in the attenuation region is a bit deeper than the uniform and graded models. In addition, the quantitative evaluation shows that the average transmittance of the tailored model is $\tau_{avg} = -9.2$ dB, corresponding to respective 53.3% and 7% improvements of the overall attenuation ability in the target frequency range, as compared to the uniform and graded counterparts.

4.2 Optimization for band-limited colored noise excitation

The second case study presented in this section deals with a band-limited colored noise excitation. The target frequency range for this case study is still assumed to be $\boldsymbol{\Psi} = [19.8, 23.3]$ as in Section 4.1. The optimization objective J_2 in Eq. (32) is used as the fitness function. Note that in many practical scenarios, the frequency spectrum of the colored noise dominates in multiple frequency ranges. Here, a colored noise with a bimodal distribution spectrum (**Figure 9**) is defined as the input excitation. This distribution profile is directly used as the weight function $\lambda(\Omega)$ to guide the optimization of the attenuation ability over this spectrum.

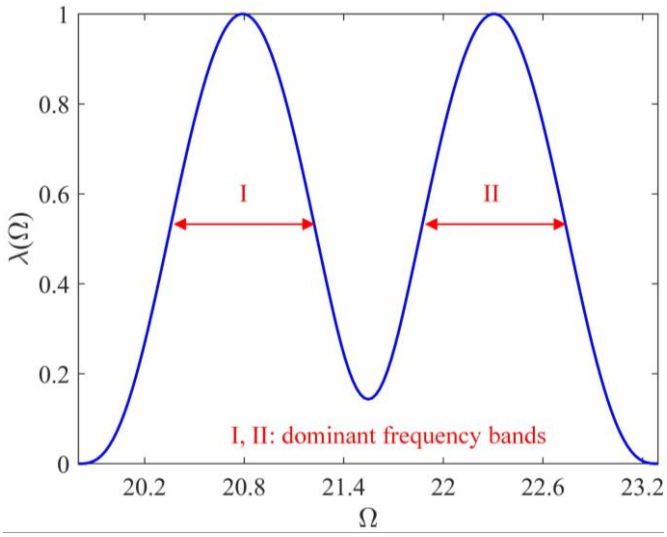

Figure 9. A bimodal distribution of the considered colored noise excitation.

Figure 10 presents the fitness value evolution during the optimization process. It is observed that the fitness value shows an overall decreasing trend. Some minor fluctuations are possibly originated from the random mutation operation. The optimal design variables determined by the optimization study are

$$\tilde{\mathbf{L}} = \begin{bmatrix} 0.00289,\ 0.00284, 0.00326, 0.00313, 0.00316, \\ 0.00273, 0.00274, 0.00319, 0.00316, 0.00279 \end{bmatrix}; \quad (37)$$
$$\tilde{R} = 0.000091$$

The transmittance responses from the piezo-meta-beam with the best fitness value in Generations 1, 11, and 100 are superposed in **Figure 10**. The transmittance inside the target frequency range is weighted by the weighting function $\lambda(\Omega)$ (Eq. (31)). It can be found that attenuation in this range is evolved to adapt to the given vibration spectrum. To clearly show the evolution of the transmittance profile during the optimization process, **Figure 11** shows the attenuation heatmaps of the piezo-meta-beam at the initial dozen and the final dozen iterations. The colored areas correspond to transmittance $\tau(\Omega) < 0$. It is observed that the transmittance profile is almost irrelevant to the vibration spectra at the initial phase (**Figure 11(a)**). After hundreds of iterations, the transmittance is tailored with attenuation ability in the dominant bands of the vibration spectrum with a bimodal distribution.

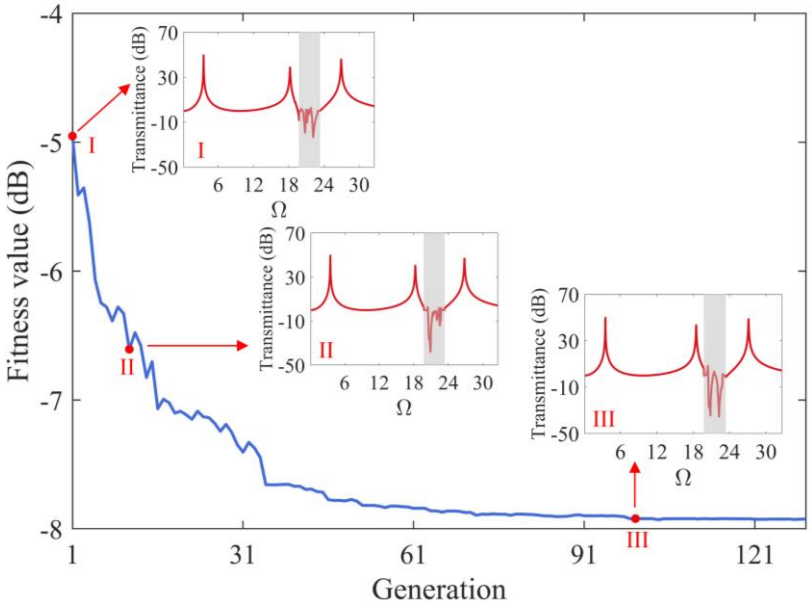

Figure 10. Fitness value evolution during the optimization process of the piezo-meta-beam subjected to the band-limited colored noise excitation with the spectrum shown in **Figure 9**. The subfigures I, II, and III show the transmittance responses of the piezo-meta-beam with the best fitness values in generations 1, 11, and 100. The grey region shaded in the subfigures denotes the target frequency region $\boldsymbol{\Psi}$. Note that the transmittances inside $\boldsymbol{\Psi}$ in the subfigures are weighted by the weighting function $\lambda(\Omega)$ in Eq. (31).

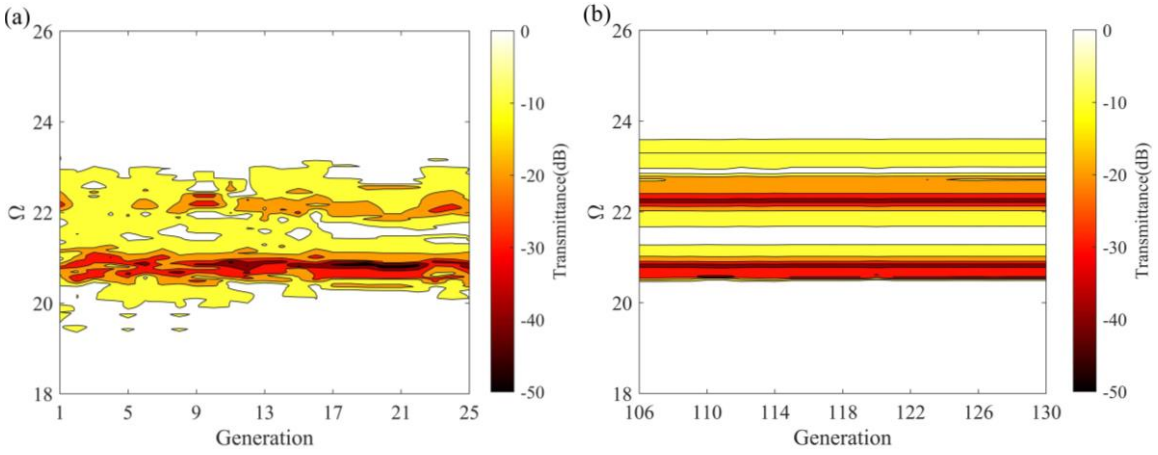

Figure 11. Attenuation heatmaps of the piezo-meta-beam subjected to the colored noise excitation with the spectrum shown in **Figure 9**: (a) Generations 1-25; (b) Generations 106-130.

Table 2. Comparison of the transmittance responses with the best fitness values from the three metamaterial models for three different band-limited colored noise excitations.

Cases	Spectrum of vibration excitation	Uniform model	Graded model	Tailored model
1	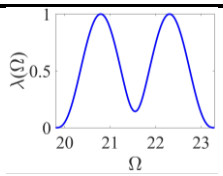	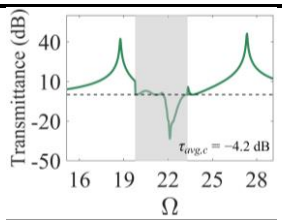	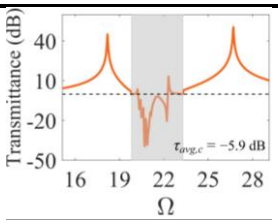	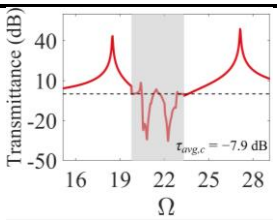
2	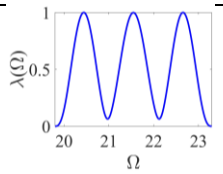	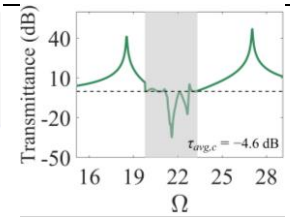	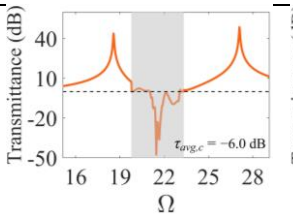	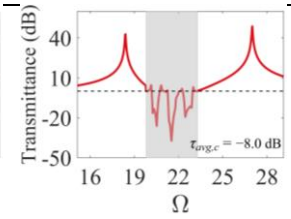
3	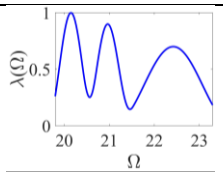	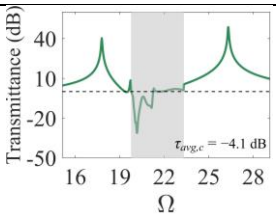	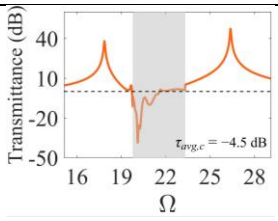	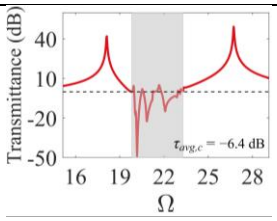

Several more case studies have been conducted to consider other band-limited colored noise excitations with different power spectral density profiles. **Table 2** summarizes the results of these additional case studies. All the models listed in **Table 2** have already been optimized using the AGA method for a fair comparison. The first column of **Table 2** illustrates the three power spectral density profiles. The rest three columns present the transmittance responses of

the uniform, graded, and tailored models, respectively. From **Table 2**, it can be found that the minimum weighted average transmittance is always obtained by the tailored model. It is also observed that the transmittance response in the attenuation region is pretty sensitive to the arrangement of the resonance frequencies of the shunt circuits. For the tailored model, the disorderly arrangement of the resonance frequencies can manipulate the transmittance profile in the attenuation region according to the power spectral density profile. To be more specific, there appear as many valleys as the number of peaks in the power spectral density profile. Furthermore, the depths of the valleys are accordingly adapted to the amplitudes of those peaks in the power spectral density profile. However, the uniform and graded models are not as intelligent as the tailored ones, i.e., the number and depths of the valleys in their transmittance plots are relatively unaccountable. To the authors' best knowledge, customizing the transmittance of a piezoelectric metamaterial according to the power spectral density profile of the excitation has not been done before by other researchers.

To quantitatively show the advantage of the tailored model, the bar chart presented in **Figure 12** compares the weighted average transmittances of the three models over the target frequency range. It is firmly confirmed that the tailored model using the proposed strategy outperforms the uniform one by approximately 56.1% − 88.1%, and the graded one by about 33.3% − 42.2%. In addition, one may notice the graded model also improves the performance of the uniform one in the first two cases, but the improvement is negligible in the last case. This shows that the graded model is only suitable for a simple vibration spectral while the AGA-based tailoring is more versatile in various vibration scenarios.

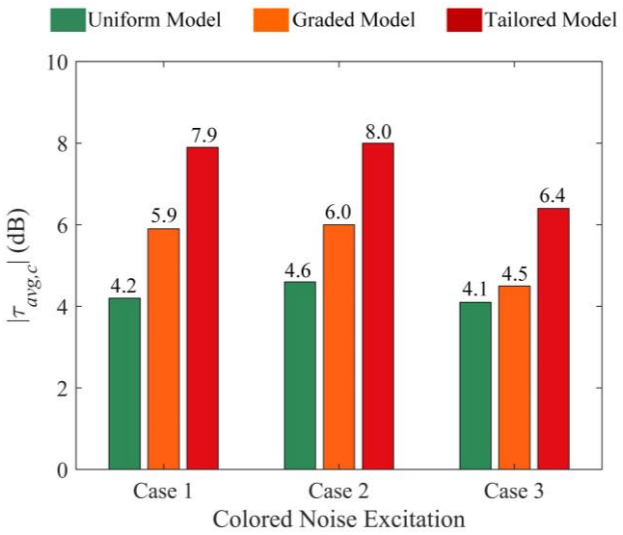

Figure 12. Comparison between the weighted average transmittances of the three models under the base excitations with different vibration spectra.

5. Conclusions

In this work, an optimal piezo-meta-beam based on an adaptive genetic algorithm (AGA) for enhancing the overall vibration attenuation ability has been presented. The cells of the metamaterial are connected to non-identical LR shunt circuits, the parameters of which are determined by the AGA-based optimization. The theoretical model for predicting the transmittance properties of the non-uniform metamaterial beam is established and verified numerically using the finite element method. The effects of the non-uniform resonance frequency array and the resistance of the shunt resonant circuits on the bandgap are discussed, which form the benchmark for tailoring the piezo-meta-beam. Subsequently, optimization strategies for two typical vibration scenarios are proposed. It has been demonstrated that the tailored piezo-meta-beam has a broader attenuation region and an enhanced average attenuation strength in the target frequency range, as compared to the uniform and graded piezo-meta-beams. Particularly, for the colored noise excitation, the values of the design variables can be adaptively adjusted to tailor the transmittance profile of the piezo-meta-beam to match the excitation spectra. This work offers a new approach for customizing the metamaterials toward optimal vibration attenuation.

Acknowledgments

This work was financially supported by a PhD scholarship from the China Scholarship Council (No. 201907000126).

References

[1] Liu Z, Zhang X, Mao Y, Zhu Y, Yang Z, Chan CT, et al. Locally resonant sonic materials. science. 2000;289:1734-6.
[2] Chen Y, Wang L. Periodic co-continuous acoustic metamaterials with overlapping locally resonant and Bragg band gaps. Applied Physics Letters. 2014;105:191907.
[3] Gao N, Hou H, Wu JH, Cheng B. Low frequency band gaps below 10 Hz in radial flexible elastic metamaterial plate. Journal of Physics D: Applied Physics. 2016;49:435501.
[4] Li J, Fan X, Li F. Numerical and experimental study of a sandwich-like metamaterial plate for vibration suppression. Composite Structures. 2020;238:111969.
[5] Meng H, Chronopoulos D, Fabro A, Elmadih W, Maskery I. Rainbow metamaterials for broadband multi-frequency vibration attenuation: Numerical analysis and experimental validation. Journal of Sound and Vibration. 2020;465:115005.
[6] Qureshi A, Li B, Tan K. Numerical investigation of band gaps in 3D printed cantilever-in-mass metamaterials. Scientific reports. 2016;6:1-10.
[7] Song K, Kim K, Hur S, Kwak J-H, Park J, Yoon JR, et al. Sound pressure level gain in an acoustic metamaterial cavity. Scientific reports. 2014;4:1-6.
[8] Jan AU, Porter R. Transmission and absorption in a waveguide with a metamaterial cavity. The Journal of the Acoustical Society of America. 2018;144:3172-80.

[9] Ning L, Wang Y-Z, Wang Y-S. Active control of elastic metamaterials consisting of symmetric double Helmholtz resonator cavities. International Journal of Mechanical Sciences. 2019;153:287-98.
[10] Yamamoto T. Acoustic metamaterial plate embedded with Helmholtz resonators for extraordinary sound transmission loss. Journal of Applied Physics. 2018;123:215110.
[11] Langfeldt F, Riecken J, Gleine W, von Estorff O. A membrane-type acoustic metamaterial with adjustable acoustic properties. Journal of Sound and Vibration. 2016;373:1-18.
[12] Lu Z, Yu X, Lau S-K, Khoo BC, Cui F. Membrane-type acoustic metamaterial with eccentric masses for broadband sound isolation. Applied Acoustics. 2020;157:107003.
[13] Chakyar SP, K. Simon S, Bindu C, Andrews J, Joseph V. Complex permittivity measurement using metamaterial split ring resonators. Journal of Applied Physics. 2017;121:054101.
[14] Hua M, Sun Y, Li M, Liu Z, Chen Y, Shi Y, et al. Electromagnetically induced transparency analog in terahertz hybrid metal–dielectric metamaterials. AIP Advances. 2021;11:065309.
[15] Fang H, Chu SCA, Xia Y, Wang KW. Programmable Self-Locking Origami Mechanical Metamaterials. Advanced Materials. 2018;30:1706311.
[16] Overvelde JT, De Jong TA, Shevchenko Y, Becerra SA, Whitesides GM, Weaver JC, et al. A three-dimensional actuated origami-inspired transformable metamaterial with multiple degrees of freedom. Nature communications. 2016;7:1-8.
[17] Gripp J, Rade D. Vibration and noise control using shunted piezoelectric transducers: A review. Mechanical Systems and Signal Processing. 2018;112:359-83.
[18] Marakakis K, Tairidis GK, Koutsianitis P, Stavroulakis GE. Shunt piezoelectric systems for noise and vibration control: a review. Frontiers in Built Environment. 2019;5:64.
[19] Thorp O, Ruzzene M, Baz A. Attenuation and localization of wave propagation in rods with periodic shunted piezoelectric patches. Smart Materials and Structures. 2001;10:979.
[20] Zhao X-N, Yang X-D. Elastic wave properties of an adaptive electromechanical metamaterial beam. Shock and Vibration. 2020;2020.
[21] Chen Y, Huang G, Sun C. Band gap control in an active elastic metamaterial with negative capacitance piezoelectric shunting. Journal of Vibration and Acoustics. 2014;136.
[22] Yi K, Collet M. Broadening low-frequency bandgaps in locally resonant piezoelectric metamaterials by negative capacitance. Journal of Sound and Vibration. 2021;493:115837.
[23] Wang G, Chen S. Large low-frequency vibration attenuation induced by arrays of piezoelectric patches shunted with amplifier–resonator feedback circuits. Smart Materials and Structures. 2015;25:015004.
[24] Wang G, Cheng J, Chen J, He Y. Multi-resonant piezoelectric shunting induced by digital controllers for subwavelength elastic wave attenuation in smart metamaterial. Smart Materials and Structures. 2017;26:025031.
[25] Li X, Chen Y, Hu G, Huang G. A self-adaptive metamaterial beam with digitally controlled resonators for subwavelength broadband flexural wave attenuation. Smart Materials and Structures. 2018;27:045015.
[26] Yi K, Matten G, Ouisse M, Sadoulet-Reboul E, Collet M, Chevallier G. Programmable metamaterials with digital synthetic impedance circuits for vibration control. Smart Materials and Structures. 2020;29:035005.
[27] Bao B, Lallart M, Guyomar D. Manipulating elastic waves through piezoelectric metamaterial with nonlinear electrical switched Dual-connected topologies. International Journal of Mechanical Sciences. 2020;172:105423.
[28] Chen Z, Xia Y, He J, Xiong Y, Wang G. Elastic-electro-mechanical modeling and analysis of piezoelectric metamaterial plate with a self-powered synchronized charge extraction circuit for vibration energy harvesting. Mechanical Systems and Signal Processing. 2020;143:106824.
[29] Fabro AT, Meng H, Chronopoulos D. Uncertainties in the attenuation performance of a multi-frequency metastructure from additive manufacturing. Mechanical Systems and Signal Processing. 2020;138:106557.
[30] Fabro AT, Beli D, Ferguson NS, Arruda JRF, Mace BR. Wave and vibration analysis of elastic metamaterial and phononic crystal beams with slowly varying properties. Wave Motion. 2021;103:102728.
[31] Banerjee A, Das R, Calius EP. Frequency graded 1D metamaterials: a study on the attenuation bands. Journal of Applied Physics. 2017;122:075101.

[32] Hu G, Austin AC, Sorokin V, Tang L. Metamaterial beam with graded local resonators for broadband vibration suppression. Mechanical Systems and Signal Processing. 2021;146:106982.
[33] Celli P, Yousefzadeh B, Daraio C, Gonella S. Bandgap widening by disorder in rainbow metamaterials. Applied Physics Letters. 2019;114:091903.
[34] Beli D, Fabro AT, Ruzzene M, Arruda JRF. Wave attenuation and trapping in 3D printed cantilever-in-mass metamaterials with spatially correlated variability. Scientific reports. 2019;9:1-11.
[35] Alshaqaq M, Erturk A. Graded multifunctional piezoelectric metastructures for wideband vibration attenuation and energy harvesting. Smart Materials and Structures. 2020;30:015029.
[36] Jian Y, Tang L, Hu G, Li Z, Aw KC. Design of Graded Piezoelectric Metamaterial Beam with Spatial Variation of Electrodes. International Journal of Mechanical Sciences. 2022:107068.
[37] Thomes RL, Beli D, Junior CDM. Space–time wave localization in electromechanical metamaterial beams with programmable defects. Mechanical Systems and Signal Processing. 2022;167:108550.
[38] Wang B, Huang Y, Zhou W, Yang Z. Metamaterial beam for flexural wave resonance rainbow trapping and piezoelectric energy harvesting. Journal of Applied Physics. 2021;129:064505.
[39] De Ponti JM, Colombi A, Ardito R, Braghin F, Corigliano A, Craster RV. Graded elastic metasurface for enhanced energy harvesting. New Journal of Physics. 2020;22:013013.
[40] Casadei F, Delpero T, Bergamini A, Ermanni P, Ruzzene M. Piezoelectric resonator arrays for tunable acoustic waveguides and metamaterials. Journal of Applied Physics. 2012;112:064902.
[41] Shao H, Chen G, He H. Elastic wave localization and energy harvesting defined by piezoelectric patches on phononic crystal waveguide. Physics Letters A. 2021;403:127366.
[42] Liu Y, Han C, Liu D. Broadband vibration suppression of graded/disorder piezoelectric metamaterials. Mechanics of Advanced Materials and Structures. 2022:1-14.
[43] Gao N, Zhang Z, Tang L, Hou H, Chen K. Optimal design of broadband quasi-perfect sound absorption of composite hybrid porous metamaterial using TLBO algorithm. Applied Acoustics. 2021;183:108296.
[44] He M-X, Ding Q. Data-driven optimization of the periodic beam with multiple acoustic black holes. Journal of Sound and Vibration. 2021;493:115816.
[45] Chelouah R, Siarry P. A continuous genetic algorithm designed for the global optimization of multimodal functions. Journal of Heuristics. 2000;6:191-213.
[46] Wu X, Li Y, Zuo S. The study of a locally resonant beam with aperiodic mass distribution. Applied Acoustics. 2020;165:107306.
[47] Meng H, Chronopoulos D, Fabro AT, Maskery I, Chen Y. Optimal design of rainbow elastic metamaterials. International Journal of Mechanical Sciences. 2020;165:105185.
[48] Shukla AK. Multi-population adaptive genetic algorithm for selection of microarray biomarkers. Neural Computing and Applications. 2020;32:11897-918.
[49] Yan C, Li M, Liu W, Qi M. Improved adaptive genetic algorithm for the vehicle Insurance Fraud Identification Model based on a BP Neural Network. Theoretical Computer Science. 2020;817:12-23.
[50] Luo C, Whitehead M, Hofmann H. Design and testing of a power electronic synthetic inductor. International journal of electronics. 2009;96:1249-64.
[51] Sugino C, Leadenham S, Ruzzene M, Erturk A. An investigation of electroelastic bandgap formation in locally resonant piezoelectric metastructures. Smart Materials and Structures. 2017;26:055029.
[52] Ji H, Qiu J, Cheng J, Inman D. Application of a negative capacitance circuit in synchronized switch damping techniques for vibration suppression. Journal of Vibration and Acoustics. 2011;133.
[53] Tang J, Wang K-W. Active-passive hybrid piezoelectric networks for vibration control: comparisons and improvement. Smart Materials and Structures. 2001;10:794.
[54] Jian Y, Hu G, Tang L, Xu J, Aw KC. A generic theoretical approach for estimating bandgap bounds of metamaterial beams. Journal of Applied Physics. 2021;130:054501.
[55] Erturk A, Inman DJ. A distributed parameter electromechanical model for cantilevered piezoelectric energy harvesters. Journal of vibration and acoustics. 2008;130:041002.
[56] Luongo A. Mode localization by structural imperfections in one-dimensional continuous systems. Journal of sound and vibration. 1992;155:249-71.

[57] Zhou W, Chen W, Chen Z, Lim C. Actively controllable flexural wave band gaps in beam-type acoustic metamaterials with shunted piezoelectric patches. European Journal of Mechanics-A/Solids. 2019;77:103807.
[58] Zheng Y, Zhang J, Qu Y, Meng G. Investigations of a piezoelectric metastructure using negative-resistance circuits to enhance the bandgap performance. Journal of Vibration and Control. 2021:10775463211010540.